

# Leading-edge vortex shedding from rotating wings

Dmitry Kolomenskiy<sup>1</sup>‡, Yossef Elimelech<sup>2</sup> and Kai Schneider<sup>3</sup>

<sup>1</sup>Centre de Recherches Mathématiques (CRM), Department of Mathematics and Statistics, McGill University, 805 Sherbrooke W., Montreal, QC, H3A 0B9, Canada

<sup>2</sup>Faculty of Aerospace Engineering, Technion-Israel Institute of Technology, Haifa 32000, Israel

<sup>3</sup>M2P2–CNRS, Université d’Aix-Marseille, 39, rue Frédéric Joliot-Curie, 13453 Marseille Cedex 13, France

E-mail: [dkolom@gmail.com](mailto:dkolom@gmail.com)

**Abstract.** The paper presents a numerical investigation of the leading-edge vortices generated by rotating triangular wings at Reynolds number  $Re = 250$ . A series of three-dimensional numerical simulations have been carried out using a Fourier pseudo-spectral method with volume penalization. The transition from stable attachment of the leading-edge vortex to periodic vortex shedding is explored, as a function of the wing aspect ratio and the angle of attack. It is found that, in a stable configuration, the spanwise flow in the recirculation bubble past the wing is due to the centrifugal force, incompressibility and viscous stresses. For the flow outside of the bubble, an inviscid model of spanwise flow is presented.

*Keywords:* Leading-edge vortex, Vortex street, Spanwise flow, Insect flight

## 1. Introduction

Vortices and vorticity production play an important role in insect flight. Insect wings have rather sharp leading edges at which the flow separates, thus producing a large amount of vorticity. The unsteadiness and the three-dimensional character of the flow lead to complex vortex dynamics and interactions with the wings. It is known that some of them have a strong positive effect on the generation of lift (e.g. Lehmann 2004). Notably, the three-dimensional character of the flow changes the dynamics of the vortex shedding from flapping or revolving wings, compared to the case of rectilinear motion, in the range of Reynolds number typical of insect flight (Liu and Kawachi 2001). Even when the wings operate at large angles of attack, the vorticity generated at the leading edge remains above the suction side (upper surface) of the wing. The pressure deficit in the recirculation bubble results in high lift at large angles of attack. This feature makes a striking contrast to the periodic vortex shedding that occurs in a two-dimensional motion. This ‘stable’ behaviour of the leading-edge vorticity is accompanied by a strong flow in the spanwise direction from the wing root towards its tip (Maxworthy 1979).

To explore these effects, we have carried out three-dimensional Navier–Stokes simulations using a pseudo-spectral method with volume penalization (Kolomenskiy *et al* 2011). These simulations are validated against experimental analysis in our earlier publication (Elimelech *et al* 2013). We consider a wing revolving about the vertical axis. The wing has a cross-section of a flat plate and its planform is triangular such that the ratio of the local radius  $r$  to the chord length  $c(r)$  is constant along the wing span (see figure 1). Lentink and Dickinson (2009a) suggest that the stability of the leading-edge vortices depends on the ratio  $r/c$ . Indeed, high aspect ratio wind turbine blades usually stall first along the distal portion of the blade, while near the hub the flow remains attached and highly three-dimensional (having a large spanwise velocity component). Lentink and Dickinson (2009a) also associate the very large local sectional lift coefficient to the fact that the flow is highly three-dimensional in the hub region. The lift coefficient at the root sections can reach very large values. Meanwhile, experiments with revolving models of insect wings by Usherwood and Ellington (2002) and recent numerical simulations by Harbig *et al* (2012) did not reveal any strong influence of the aspect ratio, probably because the shape of those wings was such that locally  $r/c$  was small enough at the sections near  $r/R = 0.5\dots 0.7$ , which produce most of the net lift force. Only the wing tip region showed sensitivity to the aspect ratio. Harbig *et al* (2013) also suggested that the flow structure is determined by the span-based Reynolds number rather than the chord-based Reynolds number. However, this scaling only holds if the spanwise velocity component is large above the wing surface.

The triangular wing shape considered in this work has the advantage that the flow in all cross-sections is characterized by the same value of the local aspect ratio  $r/c = R/C$ , where  $R$  is the wing length and  $C$  is the tip chord. Therefore, cross-sections in the middle portion of the wing operate under similar conditions. Our results indicate that very elongated wings do not generate stable leading-edge vortices, unlike less elongated

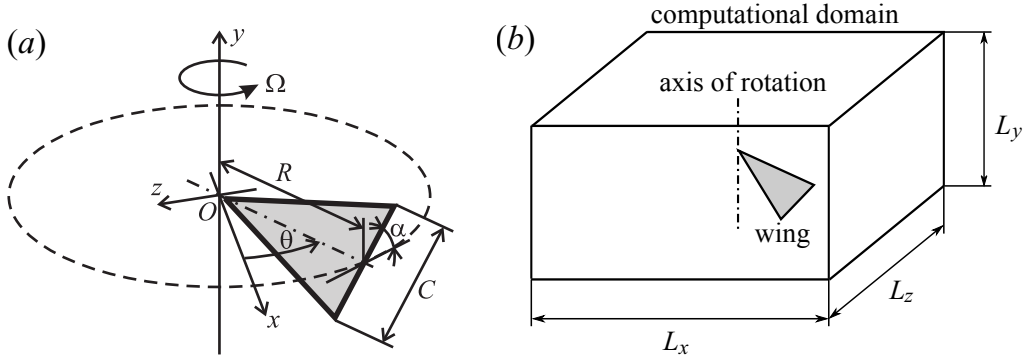


**Figure 1.** (a) Schematic diagram showing the wing rotating about the vertical axis. (b) Computational domain.

wings. We identify the marginal value of the local aspect ratio corresponding to this transition.

Moreover, it should be noted that the properties of the leading-edge vortex significantly vary as the Reynolds number varies (Shyy and Liu 2007). Our work focuses on wings operating at the Reynolds number  $Re = 250$ , representative of smaller insects, e.g. it is about 130 for a fruit fly and about 480 for a mosquito.

In section 2 we describe the flow configuration and briefly recall the numerical method. Numerical results and a potential flow model for the spanwise flow are discussed in section 3. Finally, conclusions and perspectives are presented in section 4.

## 2. Numerical setup

We consider a single wing rotating about vertical axis  $Oy$ , as shown in figure 1. The wing is a flat plate of thickness  $h = 0.12c_{0.5}$ , where  $c_{0.5}$  is the mid-span chord length. It is inclined with respect to the horizontal plane  $Oxz$  at angle  $\alpha$  that we call the angle of attack. The wing shape is triangular, such that the chord length  $c$  varies linearly with radius  $r$ :  $c(r) = 2r/\Lambda$ , where  $\Lambda$  is the aspect ratio conventionally defined as the square of the wing length divided by the the area (see, e.g. Anderson 2000). In this particular case, we have  $\Lambda/2 = R/C$ . Moreover, the local ratio  $r/c(r)$  is constant and equal to  $\Lambda/2$ .

The motion starts from rest at  $t = 0$  and the angular velocity  $\dot{\theta}$  varies like

$$\dot{\theta}/\Omega = 1 - e^{-t/\tau}. \quad (1)$$

Equation (1) results in a gradual increase of the angular velocity until it reaches 99% of its ultimate value at  $t/\tau = -\ln 0.01$ , then it remains approximately constant. The gradual increase of the velocity allows avoiding singularity of the aerodynamic force at  $t = 0$ , otherwise present if the motion starts impulsively. In order to obtain comparable vortex shedding frequencies in computations with different values of  $\Lambda$ , it is convenient to ensure that, in all cases, the mid-span section travels the same distance per unit time. This implies that the time evolution of  $\theta/(2 \arctan \Lambda/2)$  should be the same in all cases.

We satisfy that approximately by setting  $\Omega = 4/\Lambda$ . The scaling factor  $\tau = 0.4348$  is expressed in the dimensionless units explained hereunder. Thus, the angular velocity reaches 99% of its ultimate value at time  $t = 2$ , which is the same for all cases. The corresponding angular position varies between cases. In the case  $\Lambda = 4$ , it corresponds to  $\theta = 90^\circ$ , consistently with our earlier study (Elimelech *et al* 2013). In this work, we are not interested in the initial transient and our analysis of the flow only focuses on time  $t > 2$ , when the angular velocity  $\dot{\theta}$  is approximately constant in time.

The computational code operates dimensionless quantities, and it is also convenient to present the results using the same normalization. The air density is constant and equal to unity,  $\rho = 1$ . All distances are normalized to the mid-span chord length, i.e.,  $c(R/2) = c_{0.5} = 1$ . Velocities are normalized to  $\Omega R/4$ . The Reynolds number is based on these two quantities and the kinematic viscosity  $\nu$ ,

$$Re = \frac{\Omega R/2 \cdot c_{0.5}}{\nu} = \frac{2}{\nu}, \quad (2)$$

so that it is independent of  $\Lambda$ .

Our Navier–Stokes solver is described in earlier publications (Kolomenskiy *et al* 2011, Kolomenskiy and Schneider 2009) in a greater detail. The incompressible three-dimensional Navier–Stokes equations are solved using a Fourier pseudo-spectral method. The no-slip boundary condition at the wing is imposed using the volume penalization method (Angot *et al* 1999). Our approach to modelling moving obstacles is described in (Kolomenskiy and Schneider 2009). Our parallel implementation of the code is based on FFTW (Frigo and Johnson 2005) and P3DFFT (Donzis *et al* 2008) fast Fourier transform packages.

### 3. Results and discussion

#### 3.1. Vortex dynamics and aerodynamic forces

Let us first compare three numerical simulations with  $\Lambda = 4, 8$  and  $16$ . The domain sizes are, respectively,  $L_x \times L_z \times L_y = 12.75^3, 21^2 \times 10.5$  and  $34^2 \times 10.625$ . The discretization grids are uniform Cartesian. They contain  $384^3, 640^2 \times 320$  and  $1024^2 \times 320$  points, respectively. Therefore, the grid step size is approximately the same in all cases. All wings operate at  $\alpha = 30^\circ$  and  $Re = 250$ .

It is instructive to consider the vortex system of a rotating wing before analyzing the dynamics of the leading-edge vorticity. As an indicator of vortex cores, it is convenient to use the  $\lambda_2$ -criterion introduced by Jeong and Hussain (1995). The vortex is defined as the region of  $\lambda_2 < 0$ ,  $\lambda_2$  being the second largest eigenvalue of  $\mathbf{S}^2 + \mathbf{\Omega}^2$ , where  $\mathbf{S}$  and  $\mathbf{\Omega}$  are, respectively, the symmetric and antisymmetric components of the velocity gradient tensor  $\nabla \mathbf{u}$ . Note that the zero isosurface does not belong to the vortex. Iso-surfaces of  $\lambda_2 = -0.01$  (an arbitrary negative value close to zero) are shown in figure 2 for two different flows: past a low aspect-ratio wing ( $\Lambda = 4$ ) and a high aspect-ratio wing ( $\Lambda = 16$ ).

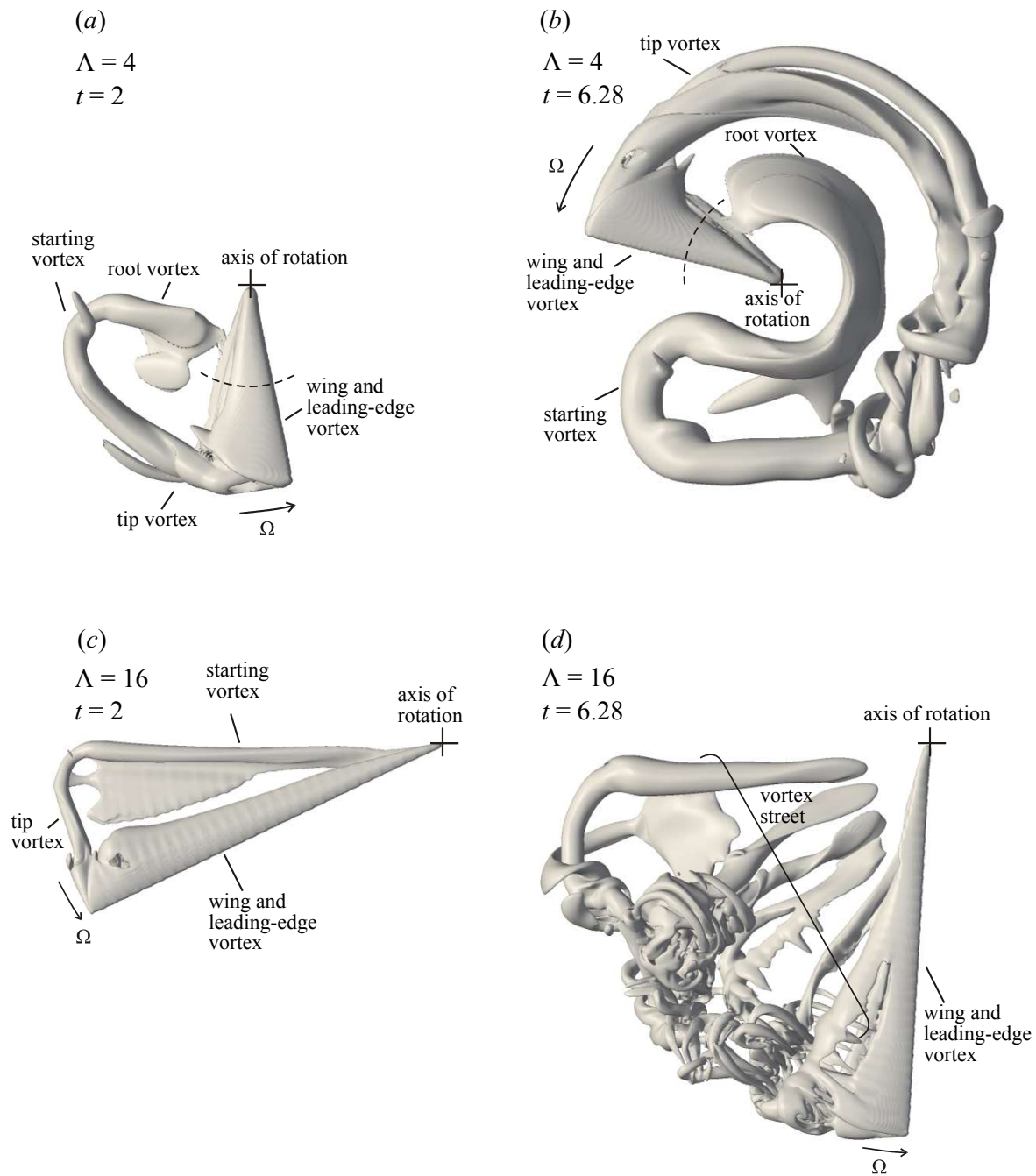


**Figure 2.** Isosurfaces of the  $\lambda_2$ -criterion for low and high aspect ratio wings: (a,b)  $\Lambda = 4$  and (c,d)  $\Lambda = 16$ . Two different time instants are shown: (a,c)  $t = 2$  and (b,d)  $t = 6.28$ . Corresponding position angles are equal to (a)  $\theta = 90^\circ$ , (b)  $335^\circ$ , (c)  $22.5^\circ$  and (d)  $83.8^\circ$ . Figures for  $\Lambda = 4$  and  $\Lambda = 16$  are not at the same scale.

Panels (a) and (b) show the wake of the low aspect ratio wing,  $\Lambda = 4$ , at two different time instants,  $t = 2$  and 6.28, respectively. Time  $t = 2$  corresponds to the end of the initial acceleration phase. The wake has a typical structure of the finite aspect ratio: a starting vortex, a tip vortex and a root vortex. The leading edge vortex is situated above the wing and has approximately conical shape, i.e., all wing sections operate under similar conditions. At  $t = 6.28$ , the leading edge vortex remains attached and travels with the wing. The wake preserves its original closed-loop structure, despite some instability near the wing tip.

Panels (c) and (d) show the wake of the high aspect ratio wing,  $\Lambda = 16$ , at the same time instants. At  $t = 2$ , the same closed-loop structure is visible as in the previous case, except that the root vorticity is now more diffuse, hence not visualized. However, by  $t = 6.28$ , the wing generates an array of radial vortices that separate from the leading and trailing edges. Those are not present in the wake of the low aspect-ratio wing. This fundamental difference is the main focus of our work.

A more detailed view of the leading-edge vorticity dynamics can be obtained from two-dimensional sections. Figure 3 shows two snapshots of the radial component of the vorticity in a cylindrical section of radius  $r/R = 0.5$ , as indicated with a dashed line in figure 2. The aspect ratio is  $\Lambda = 4$ . The flow separates from both leading and trailing edges, and two layers of counter-rotating vorticity emerge from the shear layers between the outer flow and the recirculation bubble past the wing. These vortices grow as the wing accelerates and approach their equilibrium state as the angular velocity  $\dot{\theta}$  approaches its ultimate value. Thus, at later time, the vorticity pattern displayed in figure 3(b) remains unaltered until the end of the first revolution, then it is slightly modified by the downwash velocity induced by the tip vortex. Note that, during hovering, the downwash is present if the wings flap as well as if they rotate. For flapping wings during hovering, periodic time evolution of the aerodynamic force establishes after 2 or 3 strokes (Wang *et al* 2004). Interaction of the leading-edge vortex with the wake of the preceding strokes is complex. It consists not only in the downwash effect, but also in wing-vortex interactions. This complicates the matter of the leading-edge vortex stability, since the interactions are strong and intrinsically unsteady. We follow a reductionist approach and, in this work, only focus on the development of leading-edge vortices in an undisturbed environment. Therefore, we only consider the first wing revolution. It may be conjectured that perturbations due to wing-wake interactions are an additional destabilizing secondary effect.

Mid-span radial vorticity plots in the case  $\Lambda = 16$  are shown in figure 4. At the instants shown in the figure,  $\dot{\theta}$  is close to its ultimate value  $\Omega$ . The figure clearly indicates vortex shedding. As one can see in figure 2(b), these vortices extend in the spanwise direction from  $r/R = 0.25$  to  $r/R = 1$  shortly after separation, then they are entrained by the tip vortex and roll up.

The intermediate case  $\Lambda = 8$  exhibits both scenarios, depending on the spanwise location. The vortices remain attached at  $r/R < 0.6$  and shedding occurs at  $r/R > 0.6$ , as shown in figure 5.

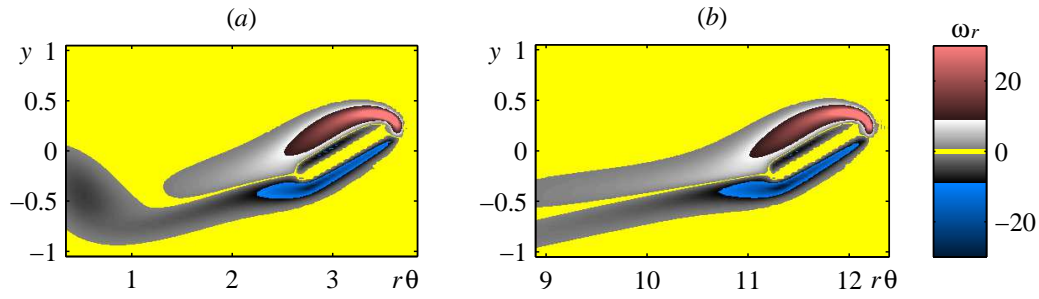


**Figure 3.** Radial component of the vorticity in the mid-span section ( $r/R = 0.5$ ) for  $\Lambda = 4$ . Time instants are (a)  $t = 2$  and (b)  $t = 6.28$ . Position angles are  $\theta = 90^\circ$  and  $335^\circ$ , respectively.

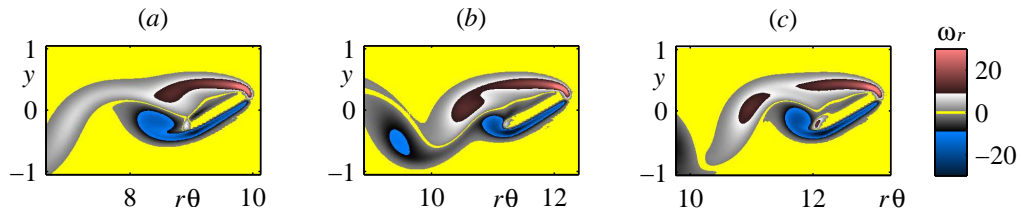


**Figure 4.** Radial component of the vorticity in the mid-span section ( $r/R = 0.5$ ) for  $\Lambda = 16$ . Time instants are (a)  $t = 5.14$ , (b)  $t = 6.28$  and (c)  $t = 6.71$ . Position angles are  $\theta = 67.5^\circ$ ,  $83.8^\circ$  and  $90^\circ$ , respectively.

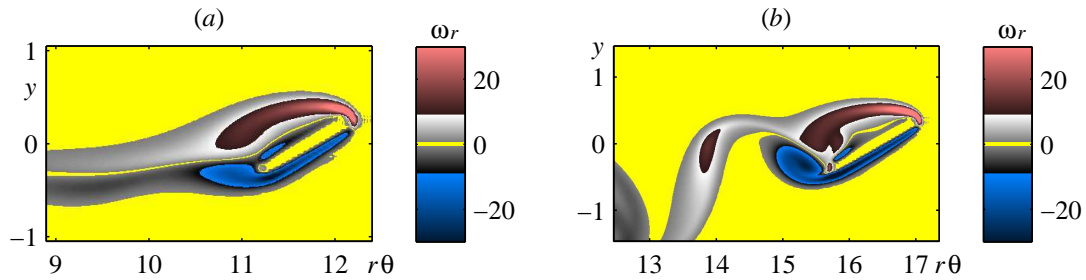


**Figure 5.** Radial component of the vorticity for  $\Lambda = 8$  in two sections: (a)  $r/R = 0.5$  and (b)  $r/R = 0.7$ . Time  $t = 6.28$ , position angle  $\theta = 167.5^\circ$ .

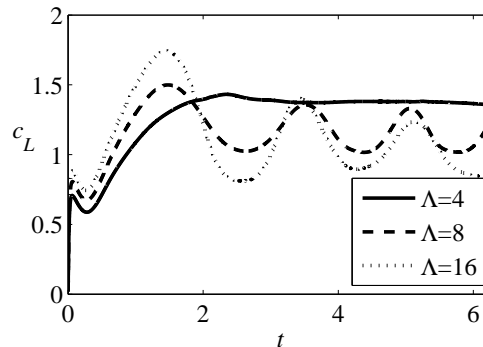


**Figure 6.** Time evolution of the lift coefficient of different wings at the angle of attack  $\alpha = 30^\circ$ .

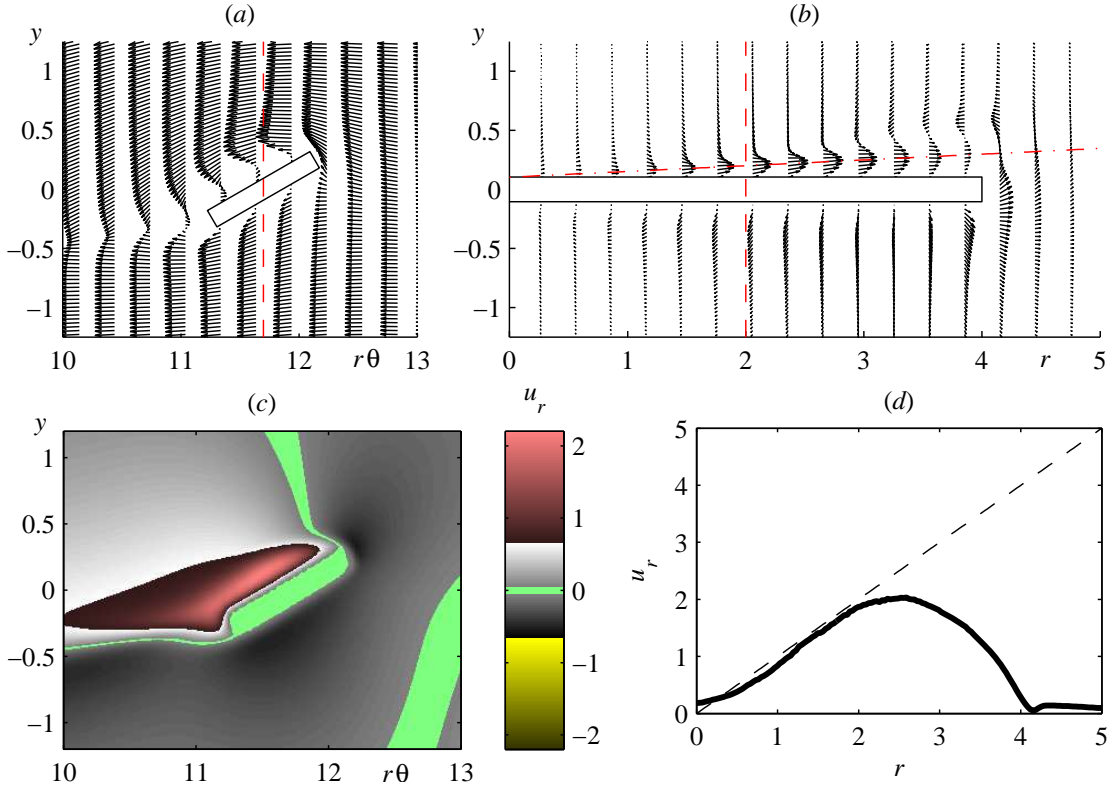


**Figure 7.** Velocity field for  $\Lambda = 4$ . In-plane velocity in (a) mid-span section and (b) spanwise section planes. Each of the two views also shows the position of the other section, indicated by a red dashed line. Vectors are at the same scale in both panels. (c) Radial velocity component in the mid-span section. (d) Radial velocity component along the horizontal red dash-dotted line indicated in figure (b). The black dashed line shows the reference circumferential velocity  $\Omega r$ . Time  $t = 6.28$ , position angle  $\theta = 335^\circ$ .

Figure 6 displays the time evolution of the lift coefficient, defined by  $c_L = 2L/\rho U_{0.65}^2 A_{wing}$ , where  $U_{0.65} = 0.65\Omega R$ ,  $A_{wing} = RC/2$ . In this notation,  $L$  is the dimensional lift force and  $\Omega$  is the angular velocity. The choice of the reference velocity  $U_{0.65}$  at  $r = 0.65R$  follows from the blade element theory: it ensures that the lift coefficient of the wing is about the same as the average section lift coefficient. The lift coefficient of the  $\Lambda = 4$  wing is almost constant after an initial transient. The  $\Lambda = 16$  wing exhibits a large overshoot during the initial acceleration, drops down to a half of the maximum value and continues oscillating with smaller amplitude. The peak values also become smaller, and the time-averaged long-term lift coefficient is lower than the one of the low aspect ratio wing. The curve corresponding to  $\Lambda = 8$  is situated in-between, because the unsteady vortex shedding occurs only from the distal portion of the wing.

The large lift coefficient of the low aspect ratio wing,  $\Lambda = 4$ , is due to the pressure deficit in the recirculation bubble (Corten 2001). This recirculation bubble is visible in figure 7(a) as a mass of fluid above the upper surface having zero relative velocity in the



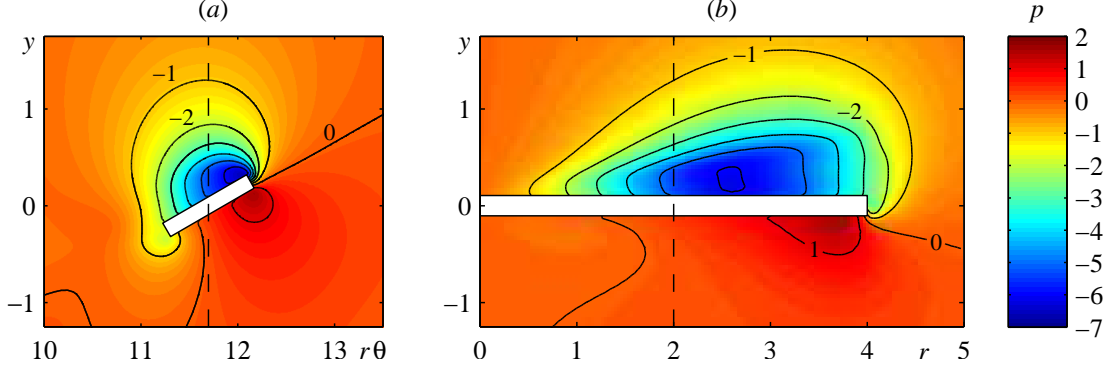


**Figure 8.** Iso-contours of the pressure for  $\Lambda = 4$ , plotted with step 1. (a) mid-span section and (b) spanwise section. Each of the two views also shows the position of the other section, indicated by a dashed line. Time  $t = 6.28$ , position angle  $\theta = 335^\circ$ .

chordwise plane. Centrifugal forces drive this fluid in the spanwise direction towards the wing tip (see figure 7b). As shown in figure 7(c), the maximum spanwise velocity is in the centre of recirculation bubble, and it is of the same order of magnitude as the local reference velocity  $\Omega r$  (see also figure 7d that shows spanwise variation of the velocity inside the bubble).

Isobars in a chordwise and in a spanwise section are shown in figure 8. Unlike in a recirculation bubble behind a bluff body in a translational motion, here the static pressure deficit on the upper surface is at least twice as large as the local (at  $r = R/2$ ) reference dynamic pressure,  $0.5\rho(\Omega R/2)^2$ . The largest negative pressure is in the vortex core near the leading edge and it gradually decreases in magnitude towards the wing's trailing edge. These observations are in agreement with Corten's theory (Corten 2001). In the spanwise direction, the pressure deficit in the recirculation bubble grows between  $r = 0$  and 2.6, then decreases towards the wing tip (see figure 8b).

Let us consider the radial component of the momentum equation in cylindrical polar coordinates, in a reference frame rotating with angular velocity  $\Omega$  about the vertical axis  $y$ :

$$\frac{\partial u_r}{\partial t} + \mathbf{u} \cdot \nabla u_r - \frac{u_\theta^2}{r} + \frac{1}{\rho} \frac{\partial p}{\partial r} - \nu \left( \nabla^2 u_r - \frac{u_r}{r^2} - \frac{2}{r^2} \frac{\partial u_\theta}{\partial \theta} \right) = 2\Omega u_\theta + \Omega^2 r. \quad (3)$$

The flow in the recirculation bubble is approximately steady, therefore  $\partial u_r / \partial t \approx 0$ . In the centre of the bubble, velocity components  $u_\theta$  and  $u_y$  and their first derivatives are small (see figure 7a). In particular, this implies that the Coriolis acceleration  $2\Omega u_\theta$  is small. Hence, in the centre of the bubble, equation (3) can be simplified to

$$u_r \frac{\partial u_r}{\partial r} + \frac{1}{\rho} \frac{\partial p}{\partial r} - \nu \left( \frac{\partial^2 u_r}{\partial y^2} + \frac{1}{r} \frac{\partial}{\partial r} (r \frac{\partial u_r}{\partial r}) + \frac{1}{r^2} \frac{\partial^2 u_r}{\partial \theta^2} - \frac{u_r}{r^2} \right) = \Omega^2 r. \quad (4)$$

Note that, in this numerical simulation, we have  $\Omega = 1$ ,  $\rho = 1$  and  $\nu = 1/125$ , in the normalized units. Let us now estimate the order of magnitude of the remaining terms. Sufficiently far from the wing tip, i.e., for  $r < 0.65R$ , the spanwise velocity varies approximately like  $u_r = A\Omega r$ , where  $A$  is of order unity, assumed constant for

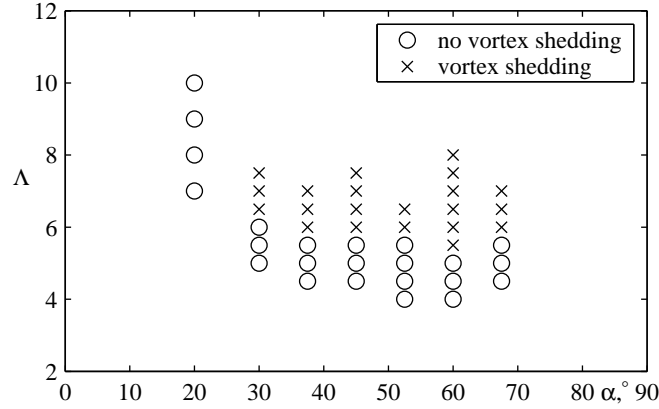


**Figure 9.** Flow regimes observed in the simulations, depending on the angle of attack and aspect ratio.

a rough estimate. Then we obtain  $u_r \frac{\partial u_r}{\partial r} \approx \Omega^2 r$ . At the same location, the pressure decreases with  $r$ . From figure 8(b), the pressure gradient term can be estimated as  $\nabla p / \rho = -B \Omega^2 r$ , where  $B$  is of order unity. Finally, figure 7(c) indicates that, at  $r = R/2 = 2$ , the vertical size of the bubble is of order 0.1 of the local chord length, suggesting that the second derivative of the velocity is of order 100 in the bubble. Computation shows that  $\partial^2 u_r / \partial y^2 \approx -300$ . Therefore, the viscous term is also of order unity. Hence, we conclude that the spanwise flow and the negative radial pressure gradient are due to the centrifugal force and viscous stresses.

### 3.2. Parametric study of vortex shedding regimes

It is of practical interest to determine the marginal value of the aspect ratio  $\Lambda_c$  such that no vortex shedding occurs if  $\Lambda < \Lambda_c$ . A series of numerical simulations have been carried out to estimate this value. In all of these computations, the domain size was set to  $L^3 = 16.8^3$  and the number of grid points to  $N^3 = 512^3$ . In the range of  $\alpha$  between 30 and 60 degrees, vortex shedding occurs at  $\Lambda > \Lambda_c = 6$ , and this value is almost independent of  $\alpha$ . When the angle of attack is sufficiently small, there is no vortex shedding regardless of the aspect ratio.

The results are summarized in figure 9, which depicts the flow regime observed in each simulation. The absolute value of the time derivative of the lift force coefficient,  $|dc_L/dt|$ , serves to indicate vortex shedding: if it exceeds 0.5 during the second half-revolution ( $\pi < \theta < 2\pi$ ), the flow regime is named “shedding”, otherwise it is called “no shedding”. This is a crude classification. Note that the flow is three-dimensional, therefore the wing tip flow separation also has some effect on the time evolution of the aerodynamic force. This effect is small when  $\alpha < 60^\circ$  (for example, see the discussion of the flow and the forces at  $\alpha = 30^\circ$  in the previous section). However, at larger  $\alpha$  it becomes comparable with the effect of vortex shedding from the leading and trailing edges. Therefore, at  $\alpha > 60^\circ$ , the criterion based on  $dc_L/dt$  fails, hence these regimes are

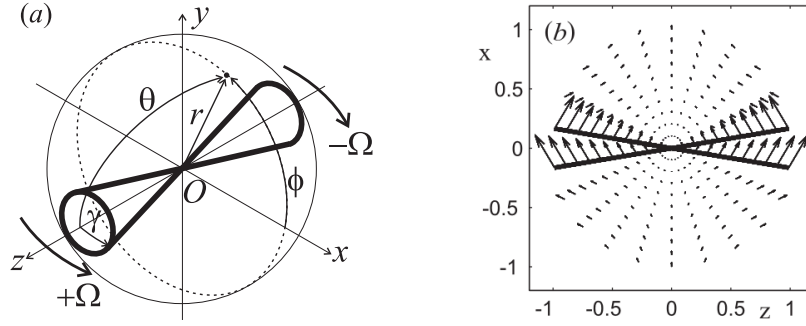


**Figure 10.** Schematic of two counter-rotating cones (a) and the potential velocity in the horizontal plane (b).

not shown in figure 9. Another possible source of unsteadiness is the spiral tip vortex. In the present study, we minimize its effect by stopping the simulations after the wing makes one complete revolution and encounters its own wake.

### 3.3. Inviscid fluid model of spanwise flow

In section 3.1, we discussed the spanwise flow in the recirculation bubble and pointed out the significance of viscous stresses in it. Along with that discussion, it is instructive to consider a simple potential flow model of a similar flow, as it provides an analytical closed form expression of the velocity field. It describes, qualitatively, the flow outside of the recirculation bubble and vortex sheets, where the flow is irrotational. For instance, it predicts a reverse spanwise flow (from wing tip to root) in the neighbourhood of the front stagnation point. This effect is seen in the numerical simulation in figure 7(c).

Let us consider the flow about two infinite coaxial cones that rotate in opposite directions, as shown in figure 10(a). Here  $\Omega$  is the angular velocity,  $\gamma$  is the angle at the vertex of the cone, and  $r, \theta, \phi$  are the polar coordinates. The geometry parameter  $\gamma$  plays a role similar to that of  $\Lambda$  in the previous section: it shows how fast the chord length (in this case the diameter) increases with the radius  $r$ .

The velocity potential  $\Phi(r, \theta, \phi)$  satisfies the following boundary value problem for Laplace's equation:

$$\begin{aligned}
 \nabla^2 \Phi &= 0, & r \in ]0, \infty[, \theta \in ]\gamma, \pi - \gamma[, \phi \in [0, 2\pi[, \\
 \frac{\partial \Phi}{r \partial \theta} &= \Omega r \cos \phi, & \text{on } \theta = \gamma, \\
 \frac{\partial \Phi}{r \partial \theta} &= -\Omega r \cos \phi, & \text{on } \theta = \pi - \gamma, \\
 \Phi &= 0 & \text{at } r = 0.
 \end{aligned} \tag{5}$$

The solution to (5) can be found in terms of the Legendre function  $Q_2^1$ ,

$$\Phi(r, \theta, \phi) = \frac{\Omega r^2 Q_2^1(\cos \theta) \cos \phi}{dQ_2^1(\cos \gamma)/d\gamma}, \tag{6}$$

where

$$Q_2^1(\cos \theta) = -\frac{3}{2} \cos \theta \sin \theta \ln \frac{1 + \cos \theta}{1 - \cos \theta} + 2 \sin \theta - \frac{\cos^2 \theta}{\sin \theta}, \quad (7)$$

Figure 10(b) displays the velocity  $\mathbf{u} = \nabla \Phi$  in the horizontal plane. Its radial component is outwards behind the cones and inwards in front of them, in agreement with the numerical simulation. The radial component, normalized to  $\Omega r$ , is

$$\frac{u_r}{\Omega r} = \frac{2Q_2^1(\cos \theta) \cos \phi}{dQ_2^1(\cos \gamma)/d\gamma}. \quad (8)$$

Its maximum value depends on the cone angle  $\gamma$  at the vertex of the cone almost linearly when  $\gamma < \pi/10$ ,

$$u_r \approx -2\gamma \Omega r \cos \phi \quad \text{on } \theta = \gamma. \quad (9)$$

At the front stagnation point,  $\phi = 0$ , the spanwise flow is towards the centre of rotation. For  $\gamma = \pi/12$ , which is about the same angle as for our smallest-aspect-ratio wing  $\Lambda = 4$  discussed in section 3.1, the velocity at  $\phi = 0$ ,  $r = 2$ ,  $\Omega = 1$  is equal to  $u_r \approx 1$ , which is somewhat larger, but comparable with, the maximum inward flow velocity displayed in figure 7(c). Of course, in a viscous flow, the velocity at the boundary is zero due to the no-slip condition, and the maximum velocity reached at the edge of the boundary layer is therefore smaller than that given by the potential flow theory. Hence, we conclude that the inward spanwise flow near the front stagnation point is a potential flow effect, unlike the outward flow in the recirculation bubble, which is a combined effect of inertia, incompressibility and viscosity.

### 3.4. Aspect ratio effect at a constant span-based Reynolds number

The numerical simulations presented in the previous sections have been carried out at a constant mid-chord-based Reynolds number  $Re$ . However, when the spanwise velocity component is large, some features of the flow field may be controlled by the span-based Reynolds number  $Re_R = \Omega R^2/\nu = 2\Lambda Re$  (Harbig *et al* 2013). In order to clarify the effect of  $Re_R$  on the transition to vortex street shedding, this section presents some results of a numerical simulation of the flow past a low aspect ratio wing ( $\Lambda = 4$ ) at  $Re = 1000$ , which yields  $Re_R = 8000$ . Note that the same value of  $Re_R$  corresponds to the flow past a high aspect ratio wing ( $\Lambda = 16$ ) discussed in section 3.1. The numerical simulation was carried out using a finer discretization grid of  $768^3$  points, as required for resolving small vortical structures due to the increased Reynolds number. The angle of attack was fixed to  $\alpha = 30^\circ$ , as in section 3.1.

Figure 11(a) displays an iso-surface of  $\lambda_2 = -0.01$ . The presence of small-scale structures in the tip vortex and partly in the leading edge vortex is the main difference from the lower Reynolds number case  $Re = 250$ ,  $\Lambda = 4$ , discussed in section 3.1. However, there are no signs of alternate vortex shedding from the leading/trailing edges and there is no vortex street in the wake, in contrast to the case  $Re = 250$ ,  $\Lambda = 16$ .

Time evolution of  $c_L$  is shown in figure 11(b). The new case  $Re = 1000$ ,  $\Lambda = 4$  is shown with a dashed line. Let us first compare it to the same wing operating

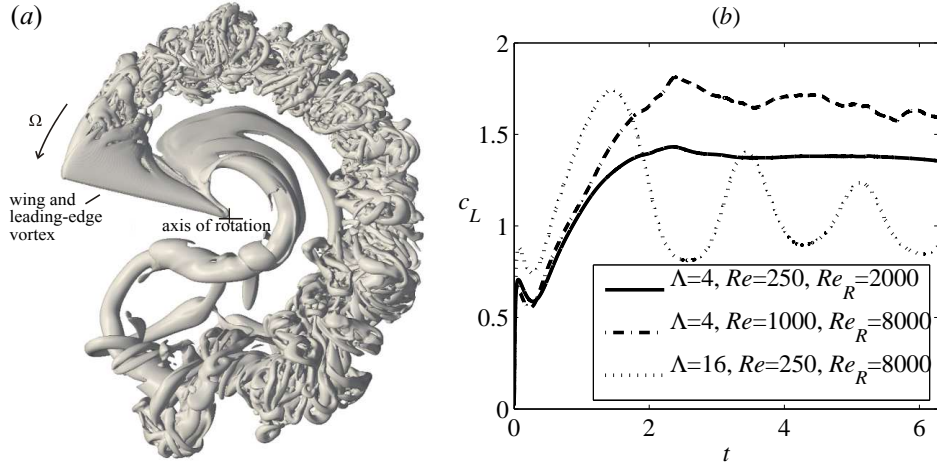


**Figure 11.** (a) Isosurfaces of the  $\lambda_2$ -criterion for  $\Lambda = 4$ ,  $Re = 1000$  at time  $t = 6.28$ . (b) Influence of  $Re$  and  $Re_R$  on the time evolution of the lift coefficient.

at  $Re = 250$ . For  $t < 1$ , there is little sensitivity of  $c_L$  to the change in  $Re$ . However, the values of  $c_L$  attained after the initial transient are about 20% larger in the higher Reynolds number case. The extra lift can be explained by the pressure deficit generated in the leading edge vortex core, which is more compact at larger  $Re$  (Shyy and Liu 2007, Maxworthy 2007). This effect is also consistent with earlier experiments (Birch *et al* 2004, Lentink and Dickinson 2009b).

There are some noticeable fluctuations in the time evolution of  $c_L$  at  $Re = 1000$ . However, their amplitude is small and there is no dominant frequency, in contrast to the case  $\Lambda = 16$ ,  $Re = 250$ . Therefore, transition to the vortex street type of wake is controlled by the aspect ratio  $\Lambda$  and the chord-based Reynolds number  $Re$  in a way that cannot be reduced to just considering the span-based Reynolds number  $Re_R = 2\Lambda Re$ .

#### 4. Conclusion and perspectives

Numerical simulation of flows past revolving wings have been carried out for a series of values of aspect ratio  $\Lambda$  and angle of attack  $\alpha$ , with the Reynolds number fixed at  $Re = 250$ .

It was found that the structure of the vortex wake significantly depends on  $\Lambda$ . If  $\Lambda > 6$  and  $\alpha > 20^\circ$ , radial vortices are shed from most part of the leading edge as well as most part of the trailing edge. This vortex shedding is accompanied by high amplitude oscillation of the aerodynamic force acting on the wing. If  $\Lambda < 5.5$ , no vortex shedding occurs and the wing generates a stable leading-edge vortex found in earlier studies (e.g. Maxworthy 1979, Liu and Kawachi 1998).

In a steady recirculation bubble past the wing, spanwise velocity in the outward direction and negative pressure gradient appear due to the action of centrifugal force and viscous stresses. This velocity is of the same order of magnitude as the wing circumferential velocity. Near the front stagnation point, the spanwise velocity is in the

opposite direction, from wing tip to root, and this is purely a potential flow effect due to incompressibility.

The structure of the leading-edge vortex also depends on the Reynolds number, therefore we only expect the above conclusions to hold if  $Re \approx 250$ . Exploring the dependence of  $\Lambda_c$  on the Reynolds number is a possible topic for future work.

## Acknowledgments

Numerical simulations were carried out using HPC resources of IDRIS, Paris, project 81664.

## References

- Anderson J D 2000 *Introduction to Flight* McGraw-Hill Series in Aeronautical and Aerospace Engineering (New York: McGraw-Hill)
- Angot P, Bruneau C H and Fabrie P 1999 A penalisation method to take into account obstacles in viscous flows *Numer. Math.* **81** 497–520
- Birch J M, Dickson W and Dickinson M H 2004 Force production and flow structure of the leading edge vortex on flapping wings at high and low Reynolds numbers *J. Exp. Biol.* **207**(7) 1063–1072
- Corten G P 2001 Flow separation on wind turbine blades. PhD thesis University of Utrecht, The Netherlands
- Donzis D A, Yeung P K and Pekurovsky D 2008 Turbulence simulations on  $O(10^4)$  processors *Proc. TeraGrid*
- Elimelech Y, Kolomenskiy D, Dalziel S B and Moffatt H K 2013 Evolution of the leading edge vortex over an accelerating rotating wing *Proc. IUTAM* **7** 233–242
- Frigo M and Johnson S G 2005 The Design and Implementation of FFTW3 *Proceedings of the IEEE* **93**(2) 216–231. Special issue on “Program Generation, Optimization, and Platform Adaptation”
- Harbig R R, Sheridan J and Thompson M C 2013 Reynolds number and aspect ratio effects on the leading-edge vortex for rotating insect wing planforms *J. Fluid Mech.* **717** 166–192
- Harbig R R, Sheridan J, Thompson M C, Ozen C A and Rockwell D 2012 Observations of Flow Structure Changes with Aspect Ratio for Rotating Insect Wing Planforms *AIAA Paper* **2012-3282** 1–8
- Jeong J and Hussain F 1995 On the identification of a vortex *J. Fluid Mech.* **285** 69–94
- Kolomenskiy D, Moffatt H K, Farge M and Schneider K 2011 Two- and three-dimensional numerical simulations of the clap–fling–sweep of hovering insects *J. Fluids Struct.* **27**(5-6) 784–791
- Kolomenskiy D and Schneider K 2009 A Fourier spectral method for the Navier–Stokes equations with volume penalization for moving solid obstacles *J. Comput. Phys.* **228** 5687–5709
- Lehmann F O 2004 The mechanisms of lift enhancement in insect flight *Naturwiss.* **91**(3) 101–122
- Lentink D and Dickinson M H 2009a Biofluiddynamic scaling of flapping, spinning and translating fins and wings *J. Exp. Biol.* **212** 2691–2704
- Lentink D and Dickinson M H 2009b Rotational accelerations stabilize leading edge vortices on revolving fly wings *J. Exp. Biol.* **212** 2705–2719
- Liu H and Kawachi K 1998 A numerical study of insect flight *J. Comput. Phys.* **146**(1) 124–156
- Liu H and Kawachi K 2001 Leading-edge vortices of flapping and rotary wings at low Reynolds number in *Prog. Astronaut. Aeronaut., Fixed and Flapping Wing Aerodynamics for Micro Air Vehicle Applications* Vol. 195 AIAA pp. 275–285
- Maxworthy T 1979 Experiments on the Weis-Fogh mechanism of lift generation by insects in hovering flight. Part 1. Dynamics of the ‘fling’ *J. Fluid Mech.* **93**(1) 47–63
- Maxworthy T 2007 The formation and maintenance of a leading-edge vortex during the forward motion of an animal wing *J. Fluid Mech.* **587** 471–475

- Shyy W and Liu H 2007 Flapping Wings and Aerodynamic Lift: The Role of Leading-Edge Vortices *AIAA J.* **45**(12) 2817–2819
- Usherwood J R and Ellington C P 2002 The aerodynamics of revolving wings. I. Model hawkmoth wings *J. Exp. Biol.* **205** 1547–1564
- Wang Z J, Birch J M and Dickinson M H 2004 Two Dimensional Mechanism for Insect Hovering *J. Exp. Biol.* **207**(3) 449–460